# Localized Intervalley Defect Excitons as Single-Photon Emitters in $WSe_2$

Lukas Linhart,[1] Matthias Paur,[2] Valerie Smejkal,[1] Joachim Burgdörfer,[1] Thomas Mueller,[2] and Florian Libisch[1]
[1]*Institute for Theoretical Physics, Vienna University of Technology, 1040 Vienna, Austria, EU*
[2]*Institute of Photonics, Vienna University of Technology, 1040 Vienna, Austria, EU*

(Received 5 April 2019; published 30 September 2019)

Single-photon emitters play a key role in present and emerging quantum technologies. Several recent measurements have established monolayer $WSe_2$ as a promising candidate for a reliable single-photon source. The origin and underlying microscopic processes have remained, however, largely elusive. We present a multiscale tight-binding simulation for the optical spectra of $WSe_2$ under nonuniform strain and in the presence of point defects employing the Bethe-Salpeter equation. Strain locally shifts excitonic energy levels into the band gap where they overlap with localized intragap defect states. The resulting hybridization allows for efficient filling and subsequent radiative decay of the defect states. We identify intervalley defect excitonic states as the likely candidate for antibunched single-photon emission. This proposed scenario is shown to account for a large variety of experimental observations including brightness, radiative transition rates, the variation of the excitonic energy with applied magnetic and electric fields as well as the variation of the polarization of the emitted photon with the magnetic field.

DOI: 10.1103/PhysRevLett.123.146401

Transition metal dichalcogenides (TMDs) have attracted considerable interest over the last decade. A direct band gap in the monolayer case [1,2], extremely large excitonic binding energies in the order of 300–500 meV [3,4] and valley as well as spin selective optical transitions due to the $D_{3h}$ symmetry [5] make these materials very promising candidates for optical devices [6,7]. Single-photon emitters (SPEs) in $WSe_2$ are among the most intriguing candidates for such future optical applications attracting considerable attention in the field of two-dimensional materials [8–25]. Single-photon emitters promising photon emission "on demand" are key building blocks for optoelectronic and photonic-based quantum-technological devices, e.g., for generating entangled photons [26].

SPEs in $WSe_2$ emit antibunched light from highly localized spots in suspended $WSe_2$ flakes featuring a narrow linewidth (down to 100 $\mu$eV) and an intricate fine structure (for a review see Ref. [27]). A large number of experimental investigations have provided key insight to help unraveling the puzzle of the microscopic origin of SPEs. The prominent observation of SPEs in regions of enhanced strain, for example, close to pillars suspending the $WSe_2$ membrane [15–17,22], points to the crucial role of locally nonuniform strain. The large defect density in $WSe_2$ also seems to play a role in the formation of SPEs [17]. The appearance of doublets in the optical spectra—i.e., single-photon emission lines with energy spacing up to 1 meV—has been attributed to the exchange interaction between excitons but the underlying mechanism has remained an open question. While in some early studies some SPEs were found to be only weakly dependent on the magnetic field, in most measurements an unexpectedly large effective $g$ factor ranging from 8 to 13 was observed [9–11,19–21,25]. Several groups observed exciton doublets with a zero field splitting in the range of 0.2 to 1 meV [9–13,16,19,21–24]. For SPEs emitting from the same region, measurements find correlated polarizations, some preferentially parallel to each other [10,12,24], while others feature pairs with orthogonal polarization, in particular for doublets [10,13,19,23,24]. Equally puzzling, both linear and quadratic Stark shifts with applied electric field were recently found for different SPEs [13,18,25]. On an even more fundamental level, there is no clear picture as to why a SPE in such a nanostructure possesses a brightness large enough to be measured at all. The latter suggests a remarkably large optical transition rate of the emitting state and a highly efficient repopulation subsequent to the photon emission. A detailed microscopic model of the processes involved has remained elusive.

In this Letter we present a multiscale simulation for $WSe_2$ with locally varying strain and in the presence of point defects. We employ a tight-binding model for the electronic structure on a single-particle level and a Bethe-Salpeter approach to account for two-particle interaction effects. From this simulation the following microscopic scenario for the origin of SPEs emerges: strongly nonuniform strain variations (e.g., near the tip of pillars [16]) result in the lowering of excitonic energies in the strained region [28] forming a weakly localized exciton [Fig. 1(a)]. In the presence of a point defect in this region, hybridization with a strongly localized defect level in the band gap leads to the formation of a novel electron-hole pair configuration termed intervalley defect exciton for which the broken valley symmetry allows efficient radiative decay

 

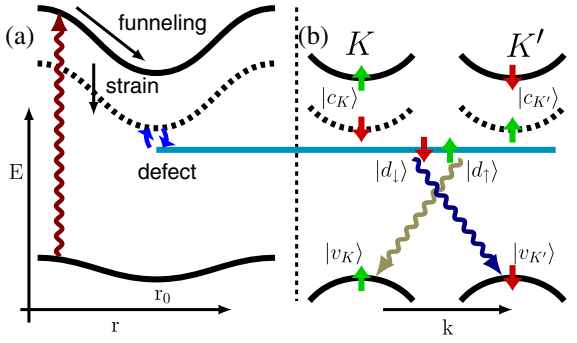


FIG. 1. Schematic illustration of single-photon emitter in $WSe_2$. (a) Real space representation: a free exciton is created (dark red arrow), strain efficiently funnels excitons with the electron in the bright (solid black line) and dark (dashed black line) conduction band down in energy towards the strain maximum near $r_0$ due to the strain-dependent band gap. Mixing of the strain-localized dark exciton with a defect state leads to the formation of a strongly localized defect exciton. (b) Reciprocal space: while dark strain-localized exciton states (dashed) remain dark, hybridization with a point defect (horizontal cyan line) breaks the valley selectivity and leads to efficient photoemission (dark blue and yellow arrows).

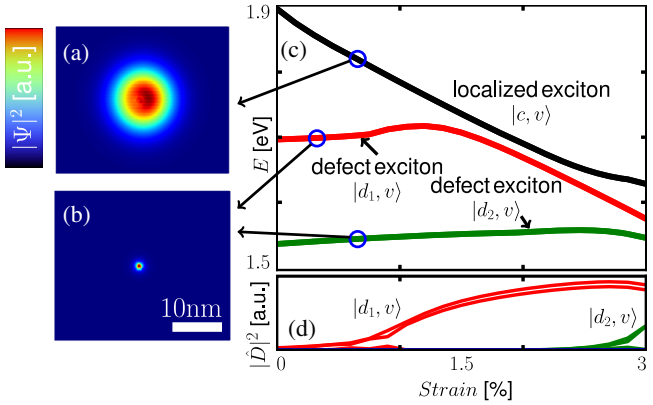


FIG. 2. Wave function and energies of strain-localized states within a single-particle picture: Real space representation of (a) a strain-localized state $|c\rangle$ emerging from the conduction band and (b) strongly localized vacancy defect state $|d\rangle$. (c) Energy shift and mixing between strain-localized exciton $|c, v\rangle$ (black) and two strongly localized defect excitons $|d_1, v\rangle$ (red) and $|d_2, v\rangle$ (green) as a function of strain. (d) Optical oscillation strength of excitonic states as function of strain. When $|c, v\rangle$ and $|d_i, v\rangle$, with defect level index $i = 1, 2$, approach each other the $|d_i, v\rangle$ exciton becomes bright. Each defect exciton spans a $4 \times 4$ subspace [Eq. 1(b)] with two optically active transitions (double lines).

[Fig. 1(b)], the key prerequisite for a SPE. Within this scenario we are able to quantitatively reproduce measurements of the SPE fine structure, magnetic-, and electric-field behavior as well as the polarization of the emitted light. The present simulation provides the theoretical underpinning of previously suggested qualitative models [16] and a consistent guide through a diverse array of seemingly contradictory observations.

The starting point of our description on the single-particle level is a multiscale approach employing density functional theory (DFT) calculations [29,30] to determine the input parameters of a subsequent tight-binding simulation [31–35] of nonuniformly strained $WSe_2$ crystals with a size of $\approx 30 \times 30$ nm$^2$, substantially larger than the suggested size of excitons [36]. This approach circumvents the need for fitting parameters by projecting onto Wannier orbitals [37,38] at different strain amplitudes and interpolating the tight-binding interactions for locally varying strain configurations (for details see the Supplemental Material [39]). The resulting single-particle eigenstates feature, indeed, strain-localized electronic excitations that originate from the bulk conduction band. We therefore denote these states by $|c\rangle$. The corresponding excitonic states also localize near the local maximum of the strain amplitude [Fig. 2(a) and Supplemental Material [39]]. The larger the strain, the more deeply the states get trapped near the center of the strain pattern [Fig. 2(c)]. We find $s$-like radially symmetric states $|c\rangle$ and $|v\rangle$ evolving from the localization of the bulk conduction and valence bands that are twofold (valley) degenerate [Fig. 2(a)]. The spatial variation of the energy of the conduction band and excitonic states [Fig. 1(a)] due to strain suggests the "funneling" of conduction band occupation into these strain-localized excitonic states [16]. The present results are found to be largely independent of the details of the strain pattern as long as the local variation of strain is sufficiently smooth such that intervalley scattering remains negligible. The highest-lying valence states are spin polarized $\langle v_K|\uparrow\rangle \approx 1$ and largely consist of atomic tungsten $d_{x^2-y^2}$ and $d_{xy}$ orbitals while the lowest-lying spin-polarized conduction band states $\langle c_K|\downarrow\rangle \approx 1$ are spanned by tungsten $d_{z^2}$ orbitals [40]. These states can be clearly associated with a well-defined valley quantum number, showing that the valley symmetry is preserved for these states under strain. Our model thus reproduces the well-known spin-valley locking in TMDs [5]. Spin-valley locking strongly influences the optical properties of $WSe_2$: in contrast to molybdenum based TMDs, the exciton in $WSe_2$ is "dark" since optical intravalley transitions are spin forbidden, with the spin allowed transition several tens of meV higher in energy, while intervalley transitions (e.g., $K \to K'$) are valley forbidden [41] [Fig. 1(b)]. Consequently, direct optical transition from the exciton to the ground state are blocked, raising intriguing questions as to the origin of the observed strong single-photon emission.

Unraveling the spin-valley locking by a local symmetry breaking through the ubiquitous presence of defects appears key to understanding and describing SPEs in $WSe_2$. Defect densities for prototypical $WSe_2$ flakes are estimated at $10^{10}$–$10^{13}$ cm$^{-2}$, resulting in approximately one defect per $10^3$–$10^5$ atoms [17,42]. Our model flake contains $\approx 30\,000$ atoms. We thus include a single

prototypical point defect. Larger strained regions in experimental flakes could include hundreds of defects. We specifically consider either a single or a double Se vacancy. While both break the in-plane translational symmetry, single Se vacancies also break the out-of-plane inversion symmetry while the latter is preserved by the double vacancy. The simulation yields strongly localized defect levels $|d_i\rangle$, $i = 1, 2$ [Fig. 2(b)], with energies below the conduction band, i.e., an electronlike state at normal doping [Fig. 2(c)]. Critical for single-photon emission is a strain-induced hybridization with the conduction band. In the following we therefore focus on the defect level $|d_1\rangle$ which shows the strongest hybridization. It features two spin states ($|d_\uparrow\rangle$, $|d_\downarrow\rangle$, where we have dropped the index 1 for brevity), but no well-defined valley polarization due to its strong localization. While also other specific defect types have been proposed as possible origins of SPEs [25,43,44], we note that the presence of any valley symmetry breaking defect seems sufficient, as long as it results in a localized state near the defect site energetically close enough to the bottom of the bulk conduction band to allow hybridization due to strain [Fig. 1(a)].

The present one-particle description of a $WSe_2$ monolayer crystal that is locally strained and decorated with a point defect is now the starting point for inclusion of two-particle interactions. For the solution of the Bethe-Salpeter equation (BSE) [45] we employ our one-particle wave functions to form a particle-hole basis $|c_j, v_i\rangle = |c\rangle^e \bigoplus |v\rangle^h$, with particle state $|c_j\rangle$ and hole state $|v_i\rangle$, where the index $(i, j)$ refers to the valleys ($K$, $K'$) the states are associated with. Since the excitonic states of interest are energetically well separated from the conduction and valence band continua and spatially localized, we restrict ourselves to the two-particle space spanned by

$$\{|c_K v_K\rangle, |c_{K'} v_K\rangle, |c_K v_{K'}\rangle, |c_{K'} v_{K'}\rangle\} \tag{1a}$$

and furthermore include defect excitons

$$\{|d_\uparrow v_K\rangle, |d_\downarrow v_K\rangle, |d_\uparrow v_{K'}\rangle, |d_\downarrow v_{K'}\rangle\}. \tag{1b}$$

We solve the BSE-type equation

$$\mathcal{H}^{\mathrm{tp}}|c_i, v_j\rangle = \mathcal{E}|c_i, v_j\rangle, \quad \mathcal{H}^{\mathrm{tp}} = (\epsilon_{c_i} - \epsilon_{v_j})\delta^i_{i'}\delta^j_{j'} + \Xi^{c_{i'},v_{j'}}_{c_i,v_j}, \tag{2}$$

where $\Xi^{c_{i'},v_{j'}}_{c_i,v_j} = W^{c_{i'},v_{j'}}_{c_i,v_j} - V^{c_{i'},v_{j'}}_{c_i,v_j}$ is the BSE interaction kernel, $W$ is the direct part, and $V$ the indirect contribution [46] (for details, see Supplemental Material [39]). The direct part $W$ of the two-particle interaction shifts the states downwards in energy by ≈100–500 meV depending on the value chosen for the dielectric constant (we use $\varepsilon/\varepsilon_0 = 10$ in the following [47]). We find no qualitative change when considering an even larger basis for solving the BSE equations (see Supplemental Material [39]). We neglect nonlocal screening present in 2D materials [48], as it does not significantly affect our results (see Supplemental Material [39]). Shifts of this order of magnitude are consistent with experimentally observed excitonic binding energies. While the indirect contribution $V$ is at least 2 orders of magnitude smaller, it is key to understand the fine structure of SPE spectra. The direct term $W$ does not lift the degeneracy since spin or valley locking allows only for nonvanishing Hartree-like diagonal terms. In the absence of defects, spin or valley locking prohibits also any nonvanishing off-diagonal contributions for $V$ for strain-localized excitonic states $\{|c, v\rangle\}$ (in contrast to bright $A$ excitons [49]). Only in the presence of defects with particle-hole states $\{|d, v\rangle\}$ off-diagonal contributions, and, thus, fine-structure splittings of the excitonic states as observed in experiment arise. The following scenario for bright excitons emerges: diagonalizing the BSE Hamiltonian [Eq. (2)] in the subspace of Eq. (1b) and thereby neglecting the hybridization between the defect state and the strain localized states $|c\rangle$ yields localized intervalley defect excitonic (IDE) states approximated by

$$|\mathrm{IDE}_\pm\rangle \approx \frac{1}{\sqrt{2}}(|d_{\uparrow(\downarrow)} v_{K(K')}\rangle \pm |d_{\downarrow(\uparrow)} v_{K'(K)}\rangle). \tag{3}$$

These IDE states appear in doublets (±) with an energy splitting of $\Delta_0 \approx 0.8$–$2$ meV, well in the experimentally observed range. Thus, the defect breaking the valley symmetry leads to the formation of doublets [Eq. (3)] with an energy spacing given by the exchange splitting. We note that inclusion of the hybridization of defect states with the strain localized states $|c\rangle$ by diagonalization of the BSE Hamiltonian in the full $8 \times 8$ space [Eq. (1)] can give rise to pairs of coupled doublets, possibly accounting for recent observations [19,24] (see Supplemental Material [39]).

The IDEs [Eq. (3)] are efficiently populated by the locally varying strain that shifts free "bulk" excitonic states $|c, v\rangle$ in energy towards defect excitonic states $|d, v\rangle$ [Fig. 1] thereby effectively funneling population into IDEs. Most importantly, the formation of defect excitons is accompanied by a dramatic increase in optical transition strength (or reduction in radiative lifetimes) when $|c, v\rangle$ and $|d, v\rangle$ approach each other in energy [Fig. 2(d)]. While the transition strength of "bulk" excitons $|c, v\rangle$, even in the presence of strain, is of the order of $10^7$ $s^{-1}$ and thus too small to serve as an efficient photon emitter, the hybridization with the defect state, which breaks the valley locking, increases the transition strength by about two orders of magnitude to $10^9$ $s^{-1}$. The corresponding radiative lifetime, which is of the order of nanoseconds, is in good agreement with experiment. These predictions are robust against variations of the defect model or the strain pattern. In turn, spatially separating the defect from the strained region decreases the transition rate as the overlap

between strain-localized excitons $|c, v\rangle$ and the excitonic defect state $|d, v\rangle$ decreases.

The present model of localized IDE states as a source of SPEs allows us to make detailed predictions for the response, both in energetic position and polarization to magnetic and electric fields without resorting to any adjustable parameter. With increasing magnetic field perpendicular to the crystal (Faraday configuration) the zero-field exciton formed near a Se vacancy defect undergoes a well-known pronounced avoided crossing [Figs. 3(c) and 3(d)] with splitting $\Delta(B) = \sqrt{\Delta_0^2 + (\mu_0 g_{\mathrm{eff}} B)^2}$ and $\Delta_0$ the zero-field splitting of the IDE doublet [Eq. (3)], in excellent agreement with several measurements of the magnetic field evolution of SPE doublets [9–13,16,17,21–25]. The linearly polarized exciton at $B = 0$ [right-handed ($\sigma^+$) and left-handed ($\sigma^-$) emission being equal] approaches circular polarization with increasing magnetic field [Figs. 3(c) and 3(d)] as for the free exciton [5]. Above $\approx$2 T these high-field excitons can again be associated with well-defined valley quantum numbers. In the high-field regime the magnetic response becomes linear. Controlled by the orbital magnetic moment of the states $|c\rangle$ and $|v\rangle$ associated with conduction (valence) band states near the $K(K')$ points $\mu = \pm 4.4\mu_0$ ($\pm 3.5\mu_0$) for $|v_{K(K')}\rangle$ with opposite sign for the two valleys, as they are connected by time reversal symmetry (similar to Ref. [50]). By contrast, a defect strongly localizes on a few atomic sites and hardly contributes to the shift with magnetic field. Therefore, the defect exciton with an effective $g$ factor of $g_{\mathrm{eff}} = 2 \times 4.4 = 8.8$ displays a much smaller (larger) Zeeman shift than the bulk intervalley exciton $|c_K, v_{K'}\rangle$ (intravalley excitons $|c_K, v_K\rangle$) with an $g_{\mathrm{eff}} = 2 \times (4.4 + 3.5) = 15.8$ ($g_{\mathrm{eff}} = 2 \times (4.4 - 3.5) = 1.8$) [see Fig. 3]. A $g$ factor of 15.8 was recently reported for localized states in valley-aligned TMD heterobilayers [51], further supporting our calculations.

We could not yet identify a systematic pattern that would connect the polarization axis with the lattice orientation or the strain gradient. However, our model allows for definite predictions for the correlation between the polarization axes of SPEs residing in close spatial proximity on the flake: the two lines from the doublet (IDE$_\pm$) have polarization axes orthogonal to each other [Fig. 3(e)] while excitons stemming from different intragap states of one single defect feature linear polarization with the polarization axis parallel to each other as the lattice distortions (and therefore the relative weights of the dipole matrix elements) are similar. These results suggest an explanation for the seemingly contradicting measurements regarding either parallel or orthogonal relative linear polarizations of spatially close SPE peaks.

Turning now to the dielectric response to an external electric field $F$ oriented perpendicular to the plane of the $WSe_2$ crystal, a wide array of different experimental results have been reported. Parametrizing the energy shift of the SPE as $E = E_0 - \mu_F F - \frac{1}{2}\alpha F^2$ with $\mu_F$ the electric dipole moment and $\alpha$ the polarizability, both linear and quadratic Stark shifts have been observed with $\mu_F$ ranging from 0.05 to 10 Debye and $\alpha$ from 0.1 to 1000 Å$^3$ [13,18,25]. The two prototypical point defects treated by our model, the single

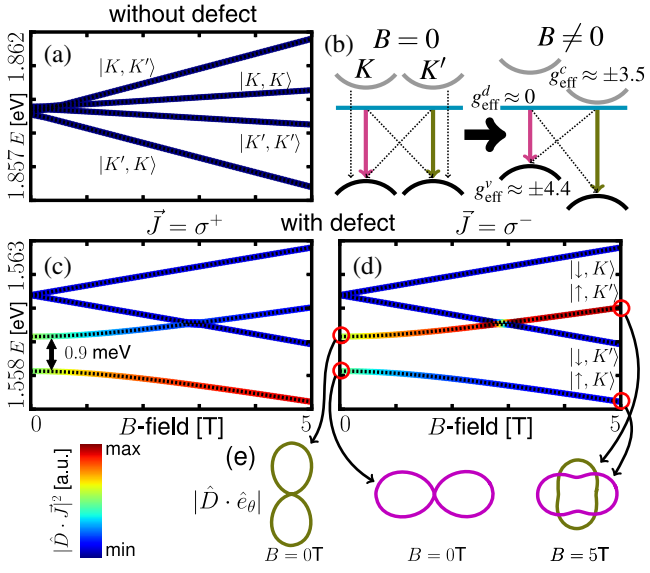


FIG. 3. Magnetic field dependence of energy and polarization of localized excitons. (a) Without a defect. (b) Schematic illustration of possible transitions and the calculated effective $g$ factor of single particle states. All transitions are dark (dashed arrows) for the defect free case, while IDEs are optically active (colored arrows). Simple Zeeman splitting of $|c_{K(K')}\rangle$ and $|v_{K(K')}\rangle$ in the absence of strain, together with the corresponding effective $g$ factors. (c)–(d) Double Se vacancy (see Supplemental Material [39] for single vacancy). (c) Right-handed [(d) left-handed] circularly polarized emission $\sigma^+$ [$\sigma^-$] as a function of the magnetic field. Color scheme of the line marks the intensity of the transition by projection on the corresponding polarization vector $\vec{J} = \sigma^+$ [$\vec{J} = \sigma^-$]. (e) Polar plot of the linear polarization of the emitted light as a function of the polarization angle.

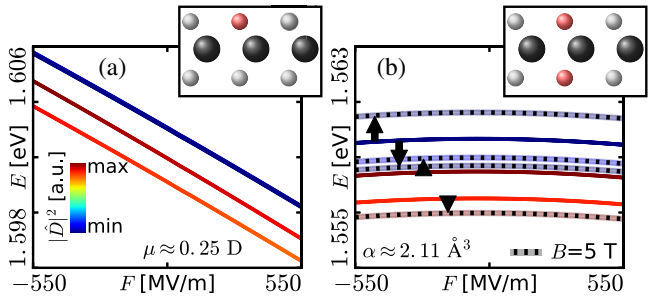


FIG. 4. Stark shift of SPE. (a) For a single Se vacancy (inversion symmetry breaking defect). (inset) Side view of the $WSe_2$ layer with a vacancy (red). Color scheme as in Fig. 3. For a double Se vacancy (symmetry preserving) defect, dashed lines are calculated with an additional magnetic field (5 T). Black arrows indicate the evolution of each state with magnetic field.

Se vacancy breaking the out-of-plane inversion symmetry and the double Se vacancy preserving this symmetry, pinpoint the origin of such diverse results. With the out-of-plane inversion symmetry broken by a single Se vacancy, we find a pronounced linear Stark shift with $\mu_F = 0.25$ D [Fig. 4(a)]. For a double vacancy we observe only a quadratic Stark effect with $\alpha = 2.1$ Å$^3$ [Fig. 4(b)]. Our results fit well to a linear-response model which estimates the Stark shift based on the density difference in the top and bottom Se layer. For the present single Se vacancy the density asymmetry is about 1%, allowing for a significantly larger $\mu_F$, well within the experimental range.

In summary, we have developed a microscopic model for bright single-photon emitters in $WSe_2$ and have identified intervalley defect excitons as likely candidates for strong photoemission. The interplay between strain and point defects enables the efficient funneling of bulk excitons near the $K(K')$ point into localized defect excitons. The broken lattice symmetry by the point defect breaks the spin-valley locking thereby opening the door to a large optical transition strength, a key prerequisite for bright photon emission. The broken valley symmetry also gives rise to an intervalley mixture of the defect exciton, explaining the splitting in doublets at zero magnetic field. The predicted dielectric and paramagnetic response of the inter-valley localized defect excitons is consistent with a large number of experimental observations. The model is also capable of predicting the variation of the polarization of the SPE photons with applied magnetic field. On a broader scope, our work suggests tailoring the interaction between delocalized and localized states in low-dimensional systems by combining strain and point defects. This concept could yield further applications in engineering the properties of low-dimensional materials. Some intriguing questions, however, remain open. Among them are the statistics of energy and brightness fluctuations of the SPE, the conclusive identification of the dominant defect type, and the kinetics of the repopulation by the funnel. Addressing these questions is key to controlling single-photon emission from $WSe_2$ for quantum optics and quantum information applications.

We acknowledge support by the TU-D doctoral program of TU Wien, as well as from the Austrian Science Fund (FWF), Project No. I-3827 N36.

[1] K. F. Mak, C. Lee, J. Hone, J. Shan, and T. F. Heinz, Phys. Rev. Lett. **105**, 136805 (2010).
[2] A. Splendiani, L. Sun, Y. Zhang, T. Li, J. Kim, C. Chim, G. Galli, and F. Wang, Nano Lett. **10**, 1271 (2010).
[3] A. Chernikov, T. C. Berkelbach, H. M. Hill, A. Rigosi, Y. Li, O. B. Aslan, D. R. Reichman, M. S. Hybertsen, and T. F. Heinz, Phys. Rev. Lett. **113**, 076802 (2014).
[4] K. He, N. Kumar, L. Zhao, Z. Wang, K. F. Mak, H. Zhao, and J. Shan, Phys. Rev. Lett. **113**, 026803 (2014).
[5] T. Cao, G. Wang, W. Han, H. Ye, C. Zhu, J. Shi, Q. Niu, P. Tan, E. Wang, B. Liu, and J. Feng, Nat. Commun. **3**, 887 (2012).
[6] T. Mueller and E. Malic, 2D Mater. Appl. **2**, 29 (2018).
[7] G. Wang, A. Chernikov, M. M. Glazov, T. F. Heinz, X. Marie, T. Amand, and B. Urbaszek, Rev. Mod. Phys. **90**, 021001 (2018).
[8] P. Tonndorf, R. Schmidt, R. Schneider, J. Kern, M. Buscema, G. A. Steele, A. Castellanos-Gomez, H. S. J. van der Zant, S. Michaelis de Vasconcellos, and R. Bratschitsch, Optica **2**, 347 (2015).
[9] S. Kumar, A. Kaczmarczyk, and B. D. Gerardot, Nano Lett. **15**, 7567 (2015).
[10] Y. He, G. Clark, J. R. Schaibley, Y. He, M. Chen, Y. Wei, X. Ding, Q. Zhang, W. Yao, X. Xu, C. Lu, and J. Pan, Nat. Nanotechnol. **10**, 497 (2015).
[11] A. Srivastava, M. Sidler, A. V. Allain, D. S. Lembke, A. Kis, and A. Imamoglu, Nat. Nanotechnol. **10**, 491 (2015).
[12] S. Kumar, M. Brotóns-Gisbert, R. Al-Khuzheyri, A. Branny, G. Ballesteros-Garcia, J. F. Sánchez-Royo, and B. D. Gerardot, Optica **3**, 882 (2016).
[13] S. Schwarz, A. Kozikov, F. Withers, J. K. Maguire, A. P. Foster, S. Dufferwiel, L. Hague, M. N. Makhonin, L. R. Wilson, A. K. Geim, K. S. Novoselov, and A. I. Tartakovskii, 2D Mater. **3**, 025038 (2016).
[14] C. Palacios-Berraquero, M. Barbone, D. M. Kara, X. Chen, I. Goykhman, D. Yoon, A. K. Ott, J. Beitner, K. Watanabe, T. Taniguchi, A. C. Ferrari, and M. Atatüre, Nat. Commun. **7**, 12978 (2016).
[15] J. Kern, I. Niehues, P. Tonndorf, R. Schmidt, D. Wigger, R. Schneider, T. Stiehm, S. Michaelis de Vasconcellos, D. E. Reiter, T. Kuhn, and R. Bratschitsch, Adv. Mater. **28**, 7101 (2016).
[16] A. Branny, S. Kumar, R. Proux, and B. D. Gerardot, Nat. Commun. **8**, 15053 (2017).
[17] Y. Luo, G. D. Shepard, J. V. Ardelean, D. A. Rhodes, B. Kim, K. Barmak, J. C. Hone, and S. Strauf, Nat. Nanotechnol. **13**, 1137 (2018).
[18] C. Chakraborty, N. R. Jungwirth, G. D. Fuchs, and A. N. Vamivakas, Phys. Rev. B **99**, 045308 (2019).
[19] X. Lu, X. Chen, S. Dubey, Q. Yao, W. Li, X. Wang, Q. Xiong, and A. Srivastava, Nat. Nanotechnol. **14**, 426 (2019).
[20] M. Koperski, K. Nogajewski, A. Arora, V. Cherkez, P. Mallet, J.-Y. Veuillen, J. Marcus, P. Kossacki, and M. Potemski, Nat. Nanotechnol. **10**, 503 (2015).
[21] C. Chakraborty, L. Kinnischtzke, K. M. Goodfellow, R. Beams, and A. N. Vamivakas, Nat. Nanotechnol. **10**, 507 (2015).
[22] C. Palacios-Berraquero, D. M. Kara, A. R.-P. Montblanch, M. Barbone, P. Latawiec, D. Yoon, A. K. Ott, M. Loncar, A. C. Ferrari, and M. Atatüre, Nat. Commun. **8**, 15093 (2017).
[23] G. Clark, J. R. Schaibley, J. Ross, T. Taniguchi, K. Watanabe, J. R. Hendrickson, S. Mou, W. Yao, and X. Xu, Nano Lett. **16**, 3944 (2016).
[24] Y. He, O. Iff, N. Lundt, V. Baumann, M. Davanco, K. Srinivasan, S. Höfling, and C. Schneider, Nat. Commun. **7**, 13409 (2016).

[25] C. Chakraborty, K. M. Goodfellow, S. Dhara, A. Yoshimura, V. Meunier, and A. N. Vamivakas, Nano Lett. **17**, 2253 (2017).
[26] D. Huber, M. Reindl, Y. Huo, H. Huang, J. S. Wildmann, O. G. Schmidt, A. Rastelli, and R. Trotta, Nat. Commun. **8**, 15506 (2017).
[27] M. Koperski, M. R. Molas, A. Arora, K. Nogajewski, A. O. Slobodeniuk, C. Faugeras, and M. Potemski, Nanophotonics **6**, 1289 (2017).
[28] S. B. Desai, G. Seol, J. S. Kang, H. Fang, C. Battaglia, R. Kapadia, J. W. Ager, J. Guo, and A. Javey, Nano Lett. **14**, 4592 (2014).
[29] G. Kresse and J. Hafner, Phys. Rev. B **47**, 558 (1993).
[30] G. Kresse and J. Hafner, Phys. Rev. B **49**, 14251 (1994).
[31] P. R. Amestoy, I. S. Duff, J. Koster, and J.-Y. L'Excellent, SIAM J. Matrix Anal. Appl. **23**, 15 (2001); P. R. Amestoy, A. Guermouche, J.-Y. L'Excellent, and S. Pralet, Parallel Comput. **32**, 136 (2006).
[32] K. J. Maschhoff and D. C. Sorensen, P_ARPACK: An Efficient Portable Large Scale Eigenvalue Package for Distributed Memory Parallel Architectures, Vol. 1184 (*Applied Parallel Computing in Industrial Problems and Optimization*) of Lecture Notes in Computer Science, edited by J. Wasniewski, J. Dongarra, K. Madsen, and D. Olesen (Springer-Verlag, Berlin Heidelberg, 1996).
[33] S. Sanvito, C. J. Lambert, J. H. Jefferson, and A. M. Bratkovsky, Phys. Rev. B **59**, 11936 (1999).
[34] D. Bischoff, F. Libisch, J. Burgdörfer, T. Ihn, and K. Ensslin, Phys. Rev. B **90**, 115405 (2014).
[35] N. Papior, N. Lorente, T. Frederiksen, A. García, and M. Brandbyge, Comput. Phys. Commun. **212**, 8 (2017).
[36] Z. Ye, T. Cao, K. O'Brien, H. Zhu, X. Yin, Y. Wang, S. G. Louie, and X. Zhang, Nature (London) **513**, 214 (2014).
[37] N. Marzari and D. Vanderbilt, Phys. Rev. B **56**, 12847 (1997).
[38] I. Souza, N. Marzari, and D. Vanderbilt, Phys. Rev. B **65**, 035109 (2001).
[39] See Supplemental Material at http://link.aps.org/supplemental/10.1103/PhysRevLett.123.146401 for details on computational methods.
[40] E. Cappelluti, R. Roldán, J. A. Silva-Guillén, P. Ordejón, and F. Guinea, Phys. Rev. B **88**, 075409 (2013).
[41] J. P. Echeverry, B. Urbaszek, T. Amand, X. Marie, and I. C. Gerber, Phys. Rev. B **93**, 121107(R) (2016).
[42] D. Edelberg, D. Rhodes, A. Kerelsky, B. Kim, J. Wang, A. Zangiabadi, C. Kim, A. Abhinandan, J. Ardelean, M. Scully, D. Scullion, L. Embon, R. Zu, E. J. G. Santos, L. Alicas, C. Marianetti, K. Barmak, X. Zhu, J. Hone, and A. N. Pasupathy, Nano Lett. **19**, 4371 (2019).
[43] S. Zhang, C. Wang, M. Li, D. Huang, L. Li, W. Ji, and S. Wu, Phys. Rev. Lett. **119**, 046101 (2017).
[44] Y. Zheng, Y. Chen, Y. Huang, P. K. Gogoi, M. Y. Li, L. Li, P. E. Trevisanutto, Q. Wang, S. J. Pennycook, A. T. Wee, and S. Y. Quek, arXiv:1811.00221.
[45] E. E. Salpeter and H. A. Bethe, Phys. Rev. **84**, 1232 (1951).
[46] E. Pavarini, E. Koch, J. Brink, and G. Sawatzky, *Quantum Material: Experiments and Theory Modeling and Simulation* (Verlag des Forschungszentrum Jülich, Jülich, Germany, 2016), Vol. 6.
[47] A. Laturia, M. L. Van de Put, and W. G. Vandenberghe, npj 2D Mater. Appl. **2**, 6 (2018).
[48] P. Cudazzo, I. V. Tokatly, and A. Rubio, Phys. Rev. B **84**, 085406 (2011).
[49] M. M. Glazov, E. L. Ivchenko, G. Wang, T. Amand, X. Marie, B. Urbaszek, and B. L. Liu, Phys. Status Solidi B **252**, 2349 (2015).
[50] A. Srivastava, M. Sidler, A. V. Allain, D. S. Lembke, A. Kis, and A. Imamoglu, Nat. Phys. **11**, 141 (2015).
[51] K. L. Seyler, P. Rivera, H. Yu, N. P. Wilson, E. L. Ray, D. G. Mandrus, J. Yan, W. Yao, and X. Xu, Nature (London) **567**, 66 (2019).